Polarization of Muons in Decay Channel

A. Van Ginneken
Fermi National Accelerator Laboratory*
P. O. Box 500, Batavia, IL 60510

November 8, 1999

Abstract

Polarization of muons in the decay channel is invesitgated. Assuming g=2 and ignoring any transverse components of $\vec{B}$ and $\vec{E}$ results in a simple transport algorithm for polarized muons. Effects of capture magnetic field strength and proton bunch length are studied.

1 Introduction

Transport of polarized muons in the decay channel of a muon collider or storage ring is investigated with the Monte Carlo code SIMUCOOL which is upgraded to include effects of polarization. The muons are followed down a 40 m long decay channel and changes of the muon's polarization—acquired at creation from a decaying pion—due to the electric and magnetic fields are examined. It is assumed for simplicity that the anomalous part of the muon magnetic moment vanishes, i.e., that g=2. Also for simplicity, muons from K–decay and 'prompt' muons—most likely from D–decay or from continuum production—are ignored. These constitute only a small fraction of the muons which can be usefully collected and their polarization would be more difficult to ascertain. (Typically, they are ignored in studies of yield and phase space density as well.) The effects of capture magnetic field strength and solenoid channel radius are studied by comparing the 'narrow'—15 cm radius and 5 $Tesla$ field—with the 'wide' case: 30 cm radius and 1.25 T field. The influence of proton bunchlength—1 $nsec$ vs 3 $nsec$—on polarization is

*Work supported by the U.S. Department of Energy under contract No. DE-AC02-76CHO3000.

illustrated along with that of target orientation (axial or tilted). Results are presented for both signs of muon collected.

Muons begin life fully polarized, i.e., with helicity of –1 for μ^+ and helicity of +1 for μ^-, in the pion restframe. Lorentz transforming this to the lab results in a loss of the perfect helicity but leaves it highly correlated to the muon's energy—which in turn produces a correlation with traversal time through the channel. This may be exploited to isolate some cut in the E–t phase space which retains a higher degree of polarization—then try to preserve it through all subsequent stages of the collider/storage ring complex. Counteracting this preservation are the time-spread of the proton beam, phase rotation in the decay channel, depolarization in the cavities, and the fact that muons are produced along the entire length of the channel. The end of the decay channel may present the best opportunity to isolate polarized muons since, in subsequent cooling, fluctuations in energy loss—restored by a (near) constant energy kick in the cavities—will tend to smear out the energy-polarization correlation. In a later installment polarization effects encountered in the cooling phase, due to both multiple scattering and re-acceleration, will be presented.

2 Polarization

Pion decay ($\pi \to \mu\nu$) results in a muon which is polarized along (for μ^-) or opposite to (μ^+) its direction of motion, denoted by a unit vector $\hat{\zeta}^*$, in the pion rest frame where the μ has fixed momentum (p^* =0.02979 GeV/c) and energy (ϵ^*=0.10978 GeV). In the laboratory, where the pion has velocity $\vec{\beta}_\pi$, the spin 4-vector is given by [1]

$$\begin{aligned} \vec{s} &= \left[\epsilon^*\hat{\zeta}^* + (\gamma_\pi - 1)\left(\epsilon^*/\beta_\pi^2\right)\left(\hat{\zeta}^* \cdot \vec{\beta}_\pi\right)\vec{\beta}_\pi + \gamma_\pi p^* \vec{\beta}_\pi\right]/m_\mu \\ s_0 &= \gamma_\pi\left[p^* + \epsilon^*\left(\hat{\zeta}^* \cdot \vec{\beta}_\pi\right)\right]/m_\mu \end{aligned} \tag{1}$$

where $\gamma_\pi = (1-\beta_\pi^2)^{-1/2}$. The muon's helicity in the lab frame is then given by the component of the spin vector $\hat{\zeta}_R$ in the muon rest frame along $\vec{p}$, its momentum in the lab

$$h = \hat{\zeta}_R \cdot \hat{p} = s_0 m_\mu/p = \gamma_\pi\left[p^* + \epsilon^*\left(\hat{\zeta}^* \cdot \vec{\beta}_\pi\right)\right]/p. \tag{2}$$

Changes in the polarization during transport are computed assuming that g=2, g being the g-factor of the muon magnetic moment. In that case propagation through an electromagnetic field $(\vec{B}, E)$ obeys the differential

equations which follow from the BMT equations [2]

$$\begin{aligned} \frac{d\vec{s}}{dt} &= \frac{e}{m_\mu \gamma_\mu}\left(\vec{s}\times\vec{B} + s_0\vec{E}\right) \\ \frac{ds_0}{dt} &= \frac{e}{m_\mu\gamma_\mu}\vec{s}\cdot\vec{E}. \end{aligned} \tag{3}$$

The error incurred by setting g=2 in the terms *included* in eq. 3 is small and is fixed trivially by multiplying the right hand sides by $(g-2)/2$ ($\simeq$0.00116). The comparable error associated with terms *omitted* is of order $\gamma^2(g-2)/2$ which, for the modest energies dealt with here, amounts to no more than a few percent of the contribution from terms that are included. However, with increasing energy the terms proportional to $g-2$ will become dominant since these are favored by a factor of γ^2 over the terms present in eq. 3. At the higher energies encountered during acceleration and storage one will naturally choose some of the standard accelerator codes to study the behavior of the muon beam—including polarization.

In the application of interest here where both magnetic field (solenoid) and electric field (cavities) are assumed to be constant and oriented along the z-axis—in regions where they do not vanish—there is further simplification. In an ideal solenoid with $\vec{B} = \hat{z}B_z$:

$$\begin{aligned} \frac{ds_x}{dz} &= \frac{e}{m_\mu\gamma_\mu}s_y B_z \\ \frac{ds_y}{dz} &= -\frac{e}{m_\mu\gamma_\mu}s_x B_z. \end{aligned} \tag{4}$$

These same equations govern the rate of change of p_x, p_y which result in the Larmor motion and are already calculated for the unpolarized case so that changes in s_x, s_y are trivially obtained. Note that $s_z, s_0, s_x^2 + s_y^2$ and thus s^2 remain constant in the solenoid and if the scalar product between $(\vec{s}, s_0)$ and $(\vec{p}, \epsilon)$ of the muon vanishes before it enters the magnet, it will remain zero during traversal. The requirement of a vanishing (Lorentz invariant) scalar product between spin and momentum four-vectors follows because it is assured in the muon rest frame where they are represented by $(\hat{s}, 0)$ and $(\vec{0}, m_\mu)$. In a cavity, it is assumed that the electric field points along the z-axis, is constant over the length of the gap and vanishes outside of it. Under these circumstances each cavity provides a fixed 'kick' to the energy of the muon while p_x and p_y remain constant. Eqs. 3 result in coupled equations between s_z and s_0

$$\frac{ds_z}{dz} = \frac{eE_z}{p_z}s_0$$

$$\frac{ds_0}{dz} = \frac{eE_z}{p_z} s_z \tag{5}$$

where p_z is the muon momentum along z. Their solution is conveniently written as

$$\begin{aligned} s_z(Z) &= s_z(0)\cosh\alpha + s_0(0)\sinh\alpha \\ s_0(Z) &= s_z(0)\sinh\alpha + s_0(0)\cosh\alpha \end{aligned} \tag{6}$$

after traversing the gap of length Z and where α is eE_z/p_z integrated over the gap, i.e.,

$$\alpha = \int_0^Z \frac{eE_z}{p_z(z)}\, dz = \ln\frac{\epsilon(Z)p_z(Z)}{\epsilon(0)p_z(0)}. \tag{7}$$

This simplifies eqs. 6 even further since

$$\cosh\alpha = \frac{1}{2}\left[\frac{\epsilon(Z)p_z(Z)}{\epsilon(0)p_z(0)} + \frac{\epsilon(0)p_z(0)}{\epsilon(Z)p_z(Z)}\right], \sinh\alpha = \frac{1}{2}\left[\frac{\epsilon(Z)p_z(Z)}{\epsilon(0)p_z(0)} - \frac{\epsilon(0)p_z(0)}{\epsilon(Z)p_z(Z)}\right] \tag{8}$$

where all quantities involved are already evaluated for the unpolarized case. From eqs. 6 it follows that the difference $s_0^2 - s_z^2$ is unchanged and since $s_x^2 + s_y^2$ is likewise constant, the algorithm for cavity traversal leaves s^2 invariant. It is easily shown that, under the above assumptions, the scalar product between spin and momentum four-vectors remains exactly at zero during acceleration, as required. In the program what happens to s_x and s_y is actually ignored and only s_z and s_0 are kept track of. The muon's helicity is then determined as $s_0 m_\mu/p$.

The rate of change of helicity passing through a cavity may be expressed as

$$\frac{dh}{dz} = m_\mu \frac{d(s_0/p)}{dz} = \frac{m_\mu e E_z}{p^2}\left(\frac{p s_z}{p_z} - \frac{\epsilon s_0}{p}\right). \tag{9}$$

It can be seen that under the conditions prevailing in this study the helicity will change only slowly. If $p_\perp$ is zero, $p = p_z$ and $p_z s_z = \epsilon s_0$ and $dh/dz = 0$. For $p_\perp \ll p_z$—as is the case in muon collection—this will only be approximately the case. Muons with the same momentum and spin vector undergo helicity changes proportional to the gradient encountered (eE_z) when traversing a cavity. Therefore, dh/dz will change sign along with eE_z and thus tend to decrease further the overall change when going through a series of cavities.

3 Calculated Yields

The scenarios simulated for the present study are the 'low-energy, long-bunch' examples from the Status Report [3] which are examined from the

viewpoint of yield and phase-space density in [4]. The target is a 36 cm long, 1 cm radius gallium target and pion generation is as predicted by MARS [5]. A 16 GeV proton beam is incident along the target axis. As in [4] the target is either along the solenoid axis or tilted at 200 $mrad$ with respect to it. Between target and main solenoid is a transition solenoid which reduces the field adiabatically [6] over a distance of 204 cm. Two solenoid channel configurations are examined: $B = 5\ Tesla$ with a radius of 15 cm and $B = 1.25\ T$, $R = 30\ cm$. Muon yield within a phase space region of $\Delta E = 0.14\ GeV$ by $\Delta cT = 8\ m$ (T is arrival time at the end of the channel) is maximized by varying the timing of the individual RF cavities and by moving this 'collection box' about in E–t–space.

In [4] the kick delivered by the first three cavities was assumed to be 6 MeV which is at variance [7] with the 2 MeV used to produce the results reported in [3]. With the lower gradient muon yields, emittances, etc., are slightly different here from those reported in [4] but do not in any way alter the conclusions reached therein. The location of the cuts adopted to maximize yield also differ somewhat from [4]: $0.118 \leq E_{kin} \leq\ 0.258\ GeV$, $183 \leq cT - z \leq 983\ cm$ for the narrow channel and $0.1 \leq E_{kin} \leq\ 0.24 GeV$, $180 \leq\ cT - z \leq\ 980\ cm$ for the wide case. As in [4], maximization is performed for the case where the target is tilted at 200 $mrad$ to the axis and where π^+/μ^+ are collected. The other cases are run with the same RF phases. The revised timings shown in columns four and five of table 1 specify where the RF sine wave vanishes (times are multiplied by c and expressed in cm) for the two cases with differing solenoid radius and field (in cm and $Tesla$) as displayed in the header. For collection of negative particles the phase is displaced by π radians. For completeness tables 2 and 3 report the updated results on muon yields. Comparison with [4] shows a slight reduction in muon yield results from lowering the acceleration gradient in the first three cavities.

4 Calculated Results on Polarization

The information one is ultimately looking for in polarization studies of this type is the distribution of polarization in the beam circulating in the collider or that of neutrinos produced in the storage ring. Simulations can point the way to devising schemes which optimize such polarizations. When they go through only part of the complex—in this case just the decay channel—information on final muon or neutrino polarization is not generated and one can only present some general results on polarization of the muons at the

Table 1: Position along decay line (z in cm), frequency (ν in MHz), maximum energy increase (ΔE in MeV) in each cavity, and timing (ct in cm) of RF cavities for $R = 15cm/B = 5T$ and $R = 30cm/B = 1.25T$ solenoids.

z	ν	ΔE	15/5	30/1.25	z	ν	ΔE	15/5	30/1.25
300	60	2.0	324.0	325.0	2220	30	4.8	2495.0	2479.2
340	60	2.0	370.0	370.4	2340	30	4.8	2628.4	2613.1
380	60	2.0	415.9	415.8	2460	30	4.8	2761.5	2747.0
420	30	4.8	461.7	461.2	2580	30	4.8	2894.3	2880.0
540	30	4.8	599.1	597.4	2700	30	4.8	3026.8	3014.7
660	30	4.8	736.3	732.8	2820	30	4.8	3159.0	3148.4
780	30	4.8	873.3	867.7	2940	30	4.8	3291.0	3282.2
900	30	4.8	1010.0	1002.7	3060	30	4.8	3422.7	3415.9
1020	30	4.8	1146.4	1137.4	3180	30	4.8	3554.1	3549.6
1140	30	4.8	1282.5	1271.9	3300	60	4.8	3685.3	3683.3
1260	30	4.8	1418.3	1406.4	3420	60	4.8	3816.2	3817.0
1380	30	4.8	1553.8	1540.7	3540	60	4.8	3946.8	3950.6
1500	30	4.8	1689.1	1674.9	3660	60	4.8	4077.1	4084.2
1620	30	4.8	1824.1	1809.1	3780	37	4.8	4207.2	4217.9
1740	30	4.8	1958.9	1943.3	3900	37	4.8	4337.0	4315.5
1860	30	4.8	2093.4	2077.3	4020	37	4.8	4466.4	4485.1
1980	30	4.8	2227.6	2211.4	4140	37	4.8	4595.7	4618.7
2100	30	4.8	2361.4	2345.3					

Table 2: Yields, restricted emittances, average momentum and *rms* spread at end of R=15 *cm*, B=5 T channel. Units are *cm* and *radian* to appropriate powers and GeV/c.

case			*total*		*within cut*					
	ns	mrad	μ	π	μ	ϵ_6^N	ϵ_T^N	ϵ_L^N	$< p >$	σ_p
+	1	0	0.384	0.145	0.214	147	1.50	65.2	0.273	0.035
—	1	0	0.354	0.115	0.207	148	1.51	64.9	0.273	0.034
+	1	200	0.389	0.106	0.229	165	1.60	64.6	0.272	0.034
—	1	200	0.375	0.095	0.226	173	1.64	64.3	0.273	0.034
+	3	0	0.384	0.144	0.195	153	1.50	67.8	0.273	0.036
—	3	0	0.353	0.115	0.188	155	1.51	68.0	0.273	0.036
+	3	200	0.387	0.108	0.209	172	1.60	67.5	0.272	0.036
—	3	200	0.375	0.095	0.207	182	1.65	67.1	0.273	0.036

Table 3: Yields, restricted emittances, average momentum and *rms* spread at end of R=30 *cm*, B=1.25 T channel. Units are *cm* and *radian* to appropriate powers and GeV/c.

case			*total*		*within cut*					
	ns	mrad	μ	π	μ	ϵ_6^N	ϵ_T^N	ϵ_L^N	$< p >$	σ_p
+	1	0	0.290	0.072	0.189	182	1.83	54.2	0.252	0.030
—	1	0	0.272	0.062	0.183	185	1.85	53.8	0.253	0.030
+	1	200	0.295	0.057	0.206	208	1.96	54.3	0.254	0.030
—	1	200	0.286	0.051	0.204	213	2.00	54.0	0.254	0.029
+	3	0	0.289	0.073	0.174	207	1.83	61.5	0.252	0.034
—	3	0	0.272	0.062	0.169	206	1.84	61.2	0.253	0.034
+	3	200	0.295	0.057	0.190	234	1.97	60.4	0.254	0.034
—	3	200	0.286	0.050	0.189	237	1.99	59.9	0.254	0.034

Table 4: Average polarization of all muons at decay, of muons able to traverse entire channel at decay and at end of channel, and of muons in acceptance cuts.

case				$\forall\mu$	μ *to reach end*			μ *within cuts*		
ch	μ	ns	mrad	decay	decay	end	depol	decay	end	depol
W	+	1	0	-0.210	-0.198	-0.189	0.044	-0.178	-0.170	0.045
W	+	1	200	-0.215	-0.202	-0.190	0.059	-0.198	-0.188	0.049
W	—	1	200	0.218	0.204	0.191	0.061	0.204	0.194	0.049
W	+	3	0	-0.210	-0.198	-0.190	0.043	-0.179	-0.171	0.048
W	+	3	200	-0.216	-0.203	-0.192	0.058	-0.200	-0.189	0.052
W	—	3	200	0.219	0.205	0.192	0.060	0.205	0.194	0.051
N	+	1	200	-0.212	-0.207	-0.198	0.047	-0.190	-0.183	0.033
N	+	3	200	-0.211	-0.207	-0.197	0.047	-0.194	-0.187	0.037

stage to which the simulations proceed. If large depolarization occurs in later stages then what is presented here may not have much predictive value and be of interest only to the general effort on how to maximize polarization or for comparison with other simulations.

Table 4 shows the average polarization of the muons at birth (π decay) and at the end of the decay channel for various cases simulated as indicated in the first four columns: narrow (N) or wide (W) channel, charge-type collected, proton pulse length, and tilt angle of target with respect to solenoid axis. The fifth column is the average polarization of all muons produced from π decay anywhere in the system. The next three columns pertain to the subset of muons which reach the end of the decay channel. They list average polarization at decay and at the end of the channel along with the depolarization (roughly of order 5%—see eq. 9) which occurs during transport through the channel. The last three columns repeat this information for the muons within the acceptance cuts. Typically, polarization is somewhat lower than that of the entire sample of surviving muons.

Table 5 presents some statistics on muons within the acceptance cuts and which satisfy an additional cut on helicity for the case of the wide channel where μ^+ are collected from a target tilted at 200 *mrad* irradiated by a 16 *GeV* proton beam with a 1 *nsec* time spread. The table shows how many muons have helicity larger (or smaller) than a a cut-off value and where they are located in E–t space. The helicity cut demands that the muon has helicity above (for $h > 0$) or below (for $h < 0$) the value

indicated in the first column of table 5. The second column shows the total number of muons per incident proton in the cut. To indicate their location in E–t-space, the third and fourth columns give the average energy and its standard deviation for this group of muons, while the fifth and sixth columns list the average value for the 'time' variable $cT - z$, where T is time and z distance to the end of the channel, and its standard deviation. The same information for the same initial conditions—except that the beam is 3 *nsec* long—is repeated in table 6. The shorter beam performs somewhat better: about 11% higher yield for muons with either $h < -0.9$ or $h > 0.9$ while their separation along the E-axis is about 26% larger. The spread in energy is also considerably smaller for the 1 *nsec* beam: 23% for negative– and 16% for positive helicities in the above ranges. There is little dependence on proton bunchlength in the numbers for time spread and separation. The advantages of the shorter beam diminish slightly as the cuts are broadened.

Fig. 1 shows curves of equal average helicity (top) and equal muon density (bottom) in E–t-space for a 1 *nsec* wide proton beam incident on a 200 *mrad* tilted gallium target where μ^+ are collected in the narrow (R=15 *cm*, B=5 *T*) channel. In the upper frame, labels identify the average helicity (indicated as $10|h|$) along each contour with dots, dot-dash, and solid representing negative, zero, and positive helicity. In the lower frame, the numerals marking each contour—when divided by 10—represent the muon density (regardless of polarization) at that point relative to the maximum density encountered in the E–t-space. Together these graphs may help identify regions in the space which—when successfully isolated—could provide muon beams of the desired degree of polarization. Both frames reveal a pattern already familiar from the scatter plots shown in [3, 4] and elsewhere, but attempt to convey more quantitative information. This figure points to one difficulty in producing polarized beams: where yield peaks, average helicity is close to zero and where average helicity is maximal, yields are small. Fig. 2 presents similar results for a 3 *nsec* beam. Comparison with fig. 1 shows again the 1 *nsec* proton beam to produce a more compact muon beam in E–t space. Figs. 3 and 4 present iso-helicity and iso-density plots for the wide channel and for which the same patterns appear even more pronounced. Fig. 5 pertains to the case where μ^- are collected in a wide channel with a 3 *nsec* proton beam. Quite naturally, it resembles fig. 4 which depicts the same case for μ^+. A relatively small amount of smoothing [8] is applied to the Monte Carlo outputs to produce figs. 1–5.

Figs. 1–5 report only the *average* helicity at each point of E–t space but convey nothing about its distribution there. To get a more complete picture of the helicity carried by the muons, the E–t space inside the cuts

Table 5: Statistics for muons in acceptance cuts plus cut in helicity, h (leftmost column) for μ^+ from **1** *nsec* proton beam on target tilted 200 *mrad* with respect to wide channel.$\langle\ E\ \rangle$, σ_E are in GeV, $\langle\ cT - z\ \rangle$, σ_t are in cm.

h-region	μ/proton	$\langle$ E $\rangle$	σ_E	$\langle$ cT-D $\rangle$	σ_t
$h < 0.$	0.1301	0.1795	0.0236	552.7	201.5
$h < -0.1$	0.1206	0.1808	0.0233	550.9	200.3
$h < -0.2$	0.1104	0.1821	0.0230	549.2	199.2
$h < -0.3$	0.0998	0.1835	0.0228	547.3	198.0
$h < -0.4$	0.0885	0.1849	0.0226	545.5	196.7
$h < -0.5$	0.0765	0.1864	0.0225	543.2	195.2
$h < -0.6$	0.0635	0.1880	0.0225	540.7	193.6
$h < -0.7$	0.0497	0.1896	0.0226	537.7	192.0
$h < -0.8$	0.0346	0.1913	0.0228	534.5	190.2
$h < -0.9$	0.0182	0.1930	0.0232	537.0	187.8
$h > 0.$	0.0747	0.1511	0.0235	587.9	220.6
$h > 0.1$	0.0655	0.1497	0.0234	589.5	221.3
$h > 0.2$	0.0567	0.1484	0.0233	591.2	221.9
$h > 0.3$	0.0483	0.1472	0.0232	592.8	222.6
$h > 0.4$	0.0403	0.1460	0.0231	594.3	223.2
$h > 0.5$	0.0326	0.1450	0.0230	596.3	224.0
$h > 0.6$	0.0254	0.1440	0.0229	598.2	224.7
$h > 0.7$	0.0185	0.1432	0.0228	600.1	225.8
$h > 0.8$	0.0119	0.1423	0.0227	602.6	226.9
$h > 0.9$	0.0058	0.1414	0.0226	605.2	228.0

Table 6: Statistics for muons in acceptance cuts plus cut in helicity, h (leftmost column) for μ^+ from **3** *nsec* proton beam on target tilted 200 *mrad* with respect to wide channel.$\langle\ E\ \rangle$, σ_E are in GeV, $\langle\ cT - z\ \rangle$, σ_t are in cm.

h-region	μ/proton	$\langle$ E $\rangle$	σ_E	$\langle$ cT-z $\rangle$	σ_t
$h < 0.$	0.1207	0.1775	0.0299	571.0	199.1
$h < -0.1$	0.1117	0.1786	0.0298	569.1	198.2
$h < -0.2$	0.1023	0.1797	0.0297	567.0	197.4
$h < -0.3$	0.0924	0.1808	0.0297	564.7	196.5
$h < -0.4$	0.0818	0.1819	0.0297	562.2	195.5
$h < -0.5$	0.0705	0.1831	0.0297	559.7	194.5
$h < -0.6$	0.0585	0.1844	0.0298	556.4	193.4
$h < -0.7$	0.0454	0.1856	0.0299	552.6	192.1
$h < -0.8$	0.0315	0.1868	0.0301	548.5	190.8
$h < -0.9$	0.0164	0.1879	0.0303	543.9	189.4
$h > 0.$	0.0687	0.1545	0.0279	610.5	215.6
$h > 0.1$	0.0601	0.1535	0.0277	612.5	216.3
$h > 0.2$	0.0520	0.1525	0.0276	614.1	217.1
$h > 0.3$	0.0442	0.1515	0.0275	615.8	218.0
$h > 0.4$	0.0368	0.1506	0.0274	617.5	218.8
$h > 0.5$	0.0298	0.1497	0.0273	619.0	219.4
$h > 0.6$	0.0232	0.1489	0.0273	620.7	220.1
$h > 0.7$	0.0168	0.1482	0.0272	622.4	220.7
$h > 0.8$	0.0108	0.1475	0.0271	624.0	221.9
$h > 0.9$	0.0052	0.1469	0.0270	625.6	222.9

is further divided into 12 rectangular subregions. In each such region the helicity distribution is histogramed and shown in figs. 6 and 7, respectively, for the 1 $nsec$ and 3 $nsec$ beams on a tilted target with μ^+ collected in the wide channel. To facilitate intercomparison, each frame in both figs. 6 and 7 has the same absolute normalization and scale of coordinate axes. Again, as expected, the shorter beam performs marginally better. In these figures, the substantial frame-to-frame variations of the helicity distribution may mean that even narrower cuts are needed to isolate relatively pure helicity muon samples.

5 Concluding Remarks

Ideally, to study the dependence of neutrino processes on helicity, one would like to isolate muons which are strongly polarized and remove the rest. Whatever strategy is ultimately adopted to bring this about, success will largely depend on having a helicity distribution which peaks at or close to $\pm$ 1 in some well defined (more or less convex shaped) region of E–t space. For example, the three regions which comprise $380 < cT - z < 980$ cm and $0.193 < E < 0.240$ cm along with the one at $380 < cT - z < 580$ cm and $0.147 < E < 0.193$ cm all have large negative helicity. Perhaps these can be combined into a single region with smoother and better optimized boundaries which one might then endeavor to isolate and transport through the rest of the system. By contrast, the lower energy/longer traversal time regime is mostly populated by high positive helicity μ^+—although their number is much lower.

The case for short bunchlength (1 *vs* 3 $nsec$) becomes marginally better when polarization is included, compared with that based on yield and phase space alone. But the benefits derived from it must still be weighted against higher costs and other difficulties with shorter bunchlength. It also remains to be analyzed how much of the polarization obtained in the decay channel can be delivered to the collider or to decay neutrinos in the storage ring. Results presented here are still a long way from these final stages making it hard to reach any conclusions on bunchlength.

Comparison with other work is not attempted here since results reported so far are few and rather sketchy. Overall levels of polarization appear similar, e.g., 0.22 as quoted in [9] compared with the entries in table 4. Other proposed phase rotation schemes such as the high energy/short bunch example of [3, 9] or use of an induction linac [9] should be examined with regard to polarization preservation. The next step will be to include changes in polar-

ization due to Coulomb scattering—such as occurs in cooling targets—into the SIMUCOOL algorithm. Eventually, polarization must be included into the subsequent stages: muon acceleration, storage, and—for the neutrino factory—decay. Simulations of these later stages will generate important feedback for devising strategies of polarization preservation in the decay channel.

My thanks to N. Holtkamp and D. Neuffer for their comments.

References

[1] S. Hayakawa, Phys. Rev. **108**, 1533 (1957).

[2] V. Bargmann, L. Michel, and V. L. Telegdi, Phys. Rev. Lett., **2**, 435 (1959). For the particular expressions employed here, see S. Y. Lee, *Spin Dynamics and Snakes in Synchrotrons*, World Scientific, Singapore (1997).

[3] C. Ankenbrandt et al., Phys. Rev. ST Accel. Beams, **2**, 081001 (1998).

[4] A. Van Ginneken, *Targetry and Collection Problems*, MuCool Note **32**, June 1999.

[5] N. V. Mokhov, *The* MARS *Code System User's Guide, version 13 (95)*, FNAL-FN-628 (1995).

[6] N. V. Mokhov, R. J. Noble, and A. Van Ginneken, *Target and Collection Optimization for Muon Colliders*, AIP Conf. Proc. *372*, 61 (1996).

[7] My thanks to Harold Kirk for pointing out this discrepancy.

[8] A. Van Ginneken, Nucl. Inst. Meth. **A305**, 453 (1991); —, FNAL-FN-675 (1998).

[9] $\mu^+\mu^-$ *Collider. A Feasibility Study.* J.C. Gallardo, Ed., BNL-52503, Fermilab-Conf-96/092, LBNL-38946 (1996); R.B. Palmer, *Neutrino Factory Draft Parameters*, MuCool Note **46**, August 1999; V. Balbekov, *The Optimization of Phase Rotation using an Induction Linac*, MuCool Note **63**, October 1999.

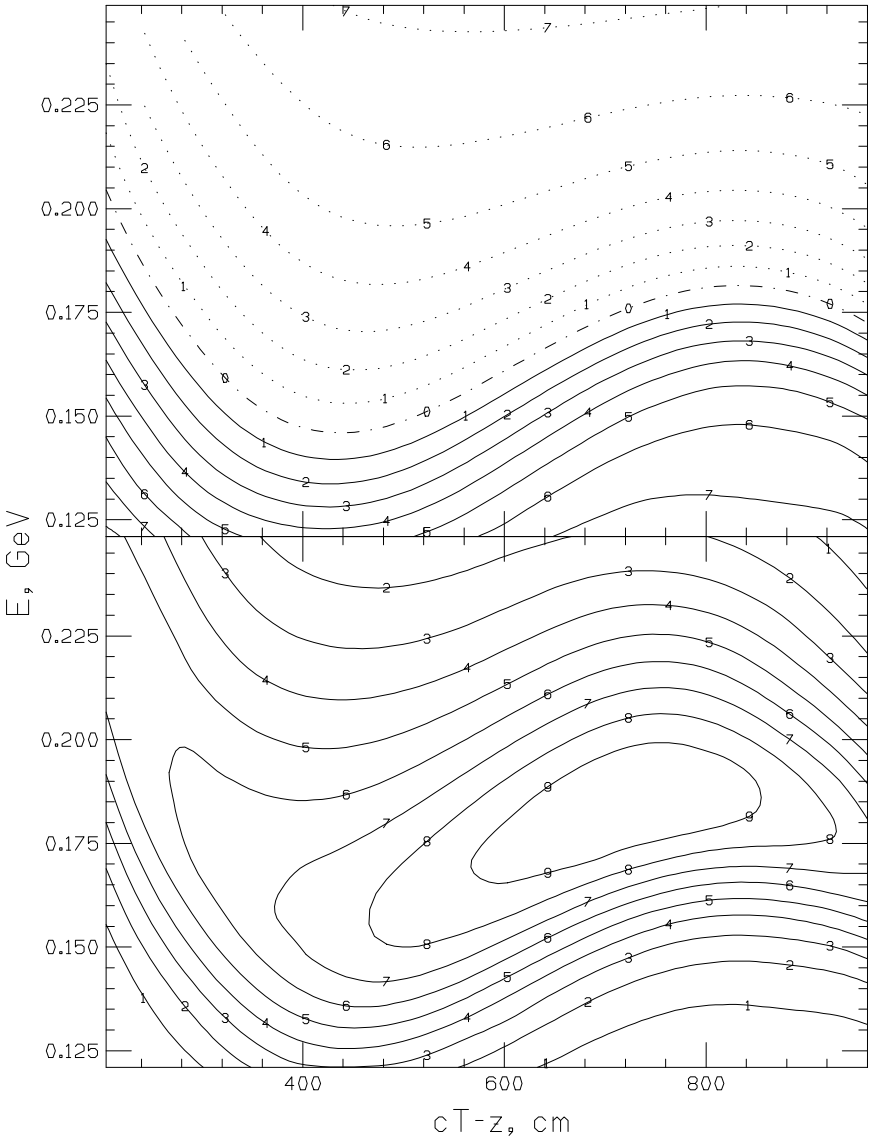

Figure 1: **Top** Contours of average helicity in E—t region of acceptance cuts for μ^+ collected in *narrow* channel with 1 *nsec* long proton beam incident on tilted target. Dotted curves represent negative helicities, solid curves positive— and dot-dash zero helicity. Label on each curve—when divided by 10—identifies average helicity at that point (e.g., the solid curve marked 2 corresponds to h=0.2, dotted curve 5 to h=–0.5). **Bottom** Contours of equal muon density. Label on each curve—when divided by 10—identifies muon density at that point relative to maximum (e.g., along curve labeled 7 muon density is 0.7 times the maximum density.

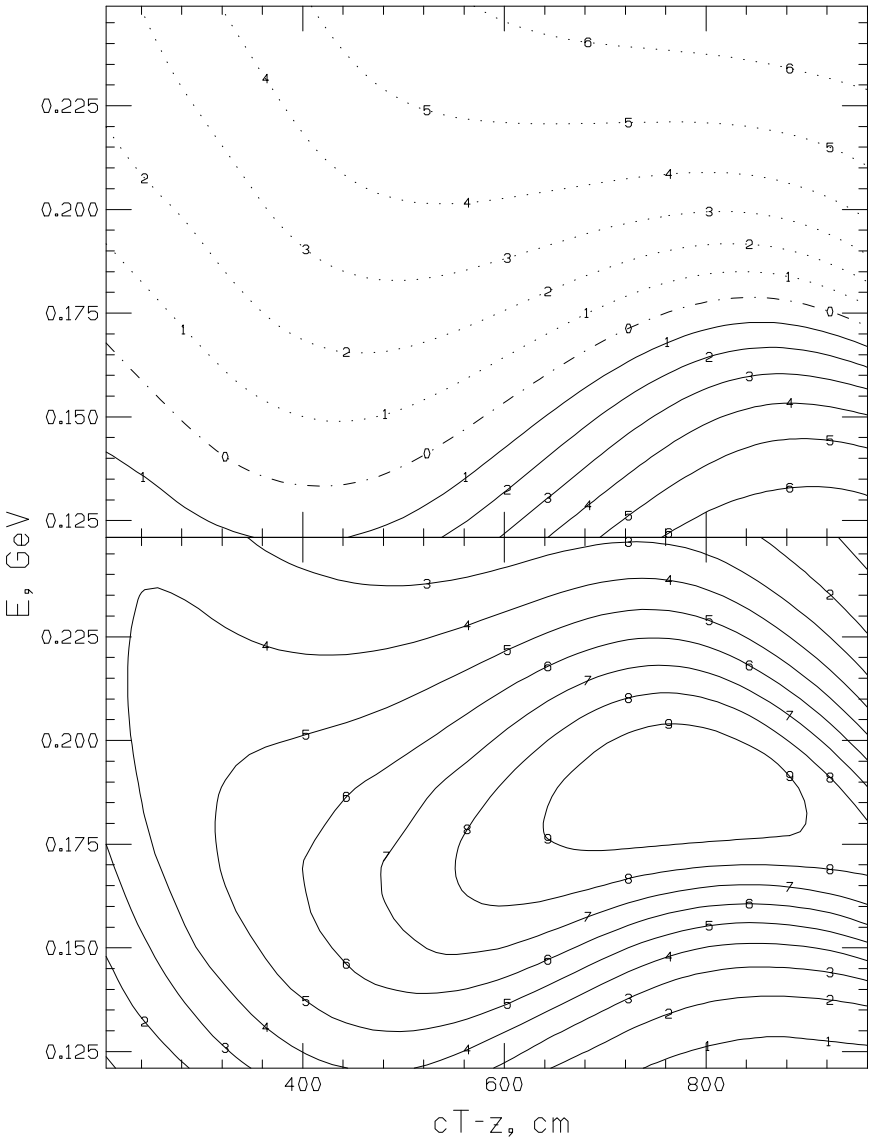

Figure 2: **Top** Contours of average helicity in E—t region of acceptance cuts for μ^+ collected in *narrow* channel with 3 *nsec* long proton beam incident on tilted target. **Bottom** Contours of equal muon density. Curves are labeled as in fig. 1

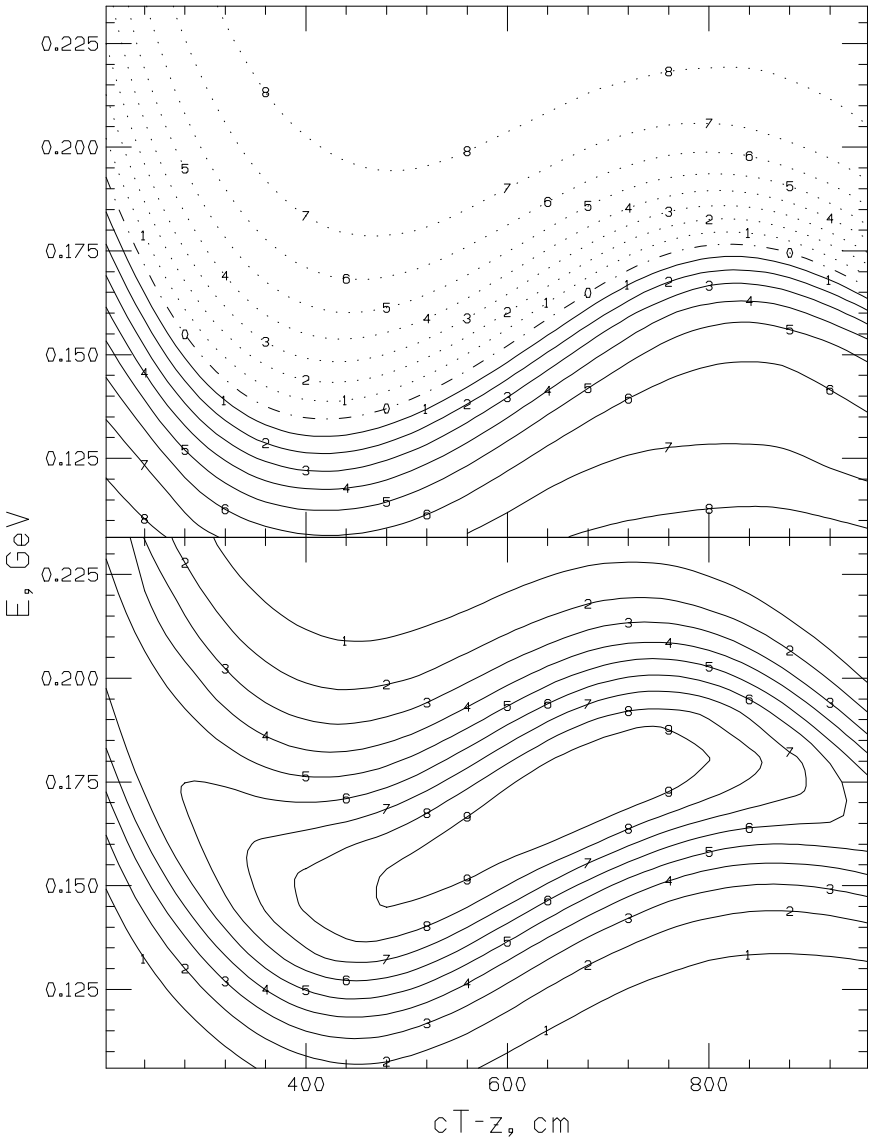

Figure 3: **Top** Contours of average helicity in E—t region of acceptance cuts for μ^+ collected in *wide* channel with 1 *nsec* long proton beam incident on tilted target. **Bottom** Contours of equal muon density. Curves are labeled as in fig. 1

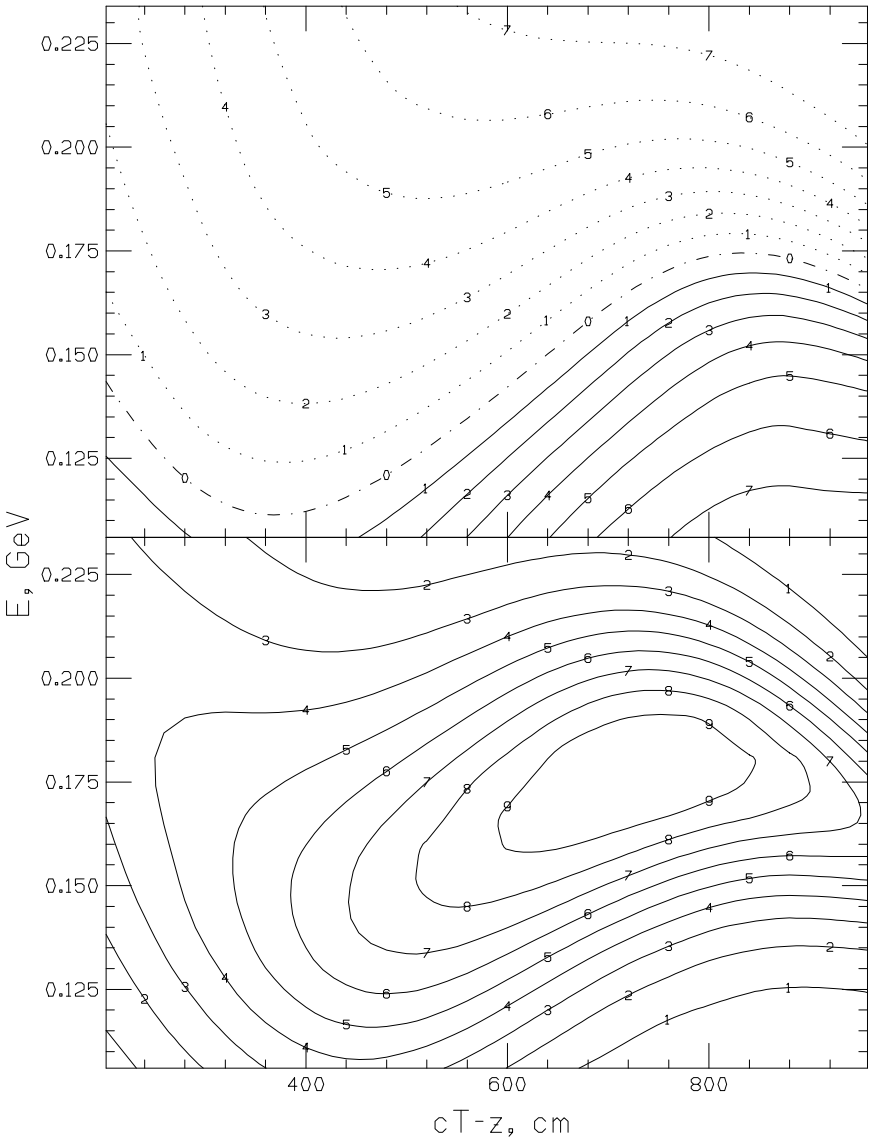

Figure 4: **Top** Contours of average helicity in E—t region of acceptance cuts for μ^+ collected in *wide* channel with 3 *nsec* long proton beam incident on tilted target. **Bottom** Contours of equal muon density. Curves are labeled as in fig. 1

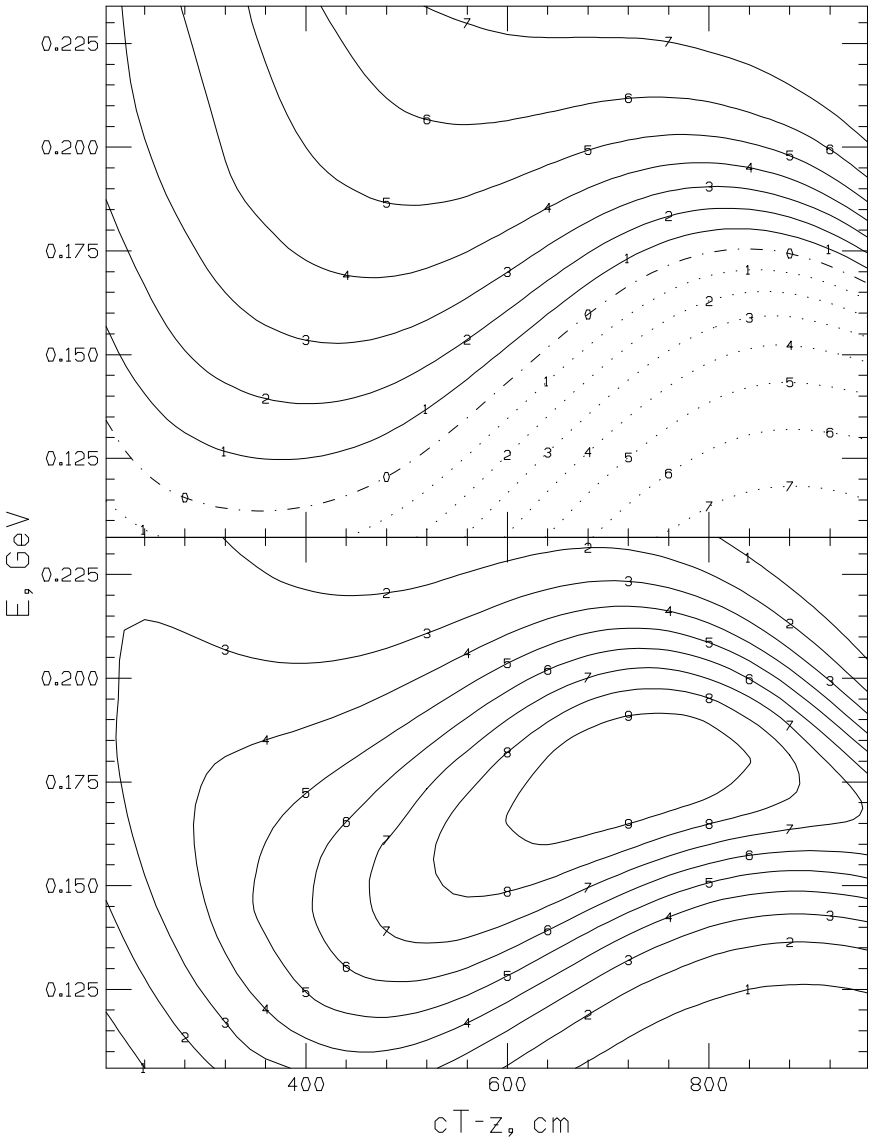

Figure 5: **Top** Contours of average helicity in E—t region of acceptance cuts for μ^- collected in *wide* channel with 3 *nsec* long proton beam incident on tilted target. **Bottom** Contours of equal muon density. Curves are labeled as in fig. 1

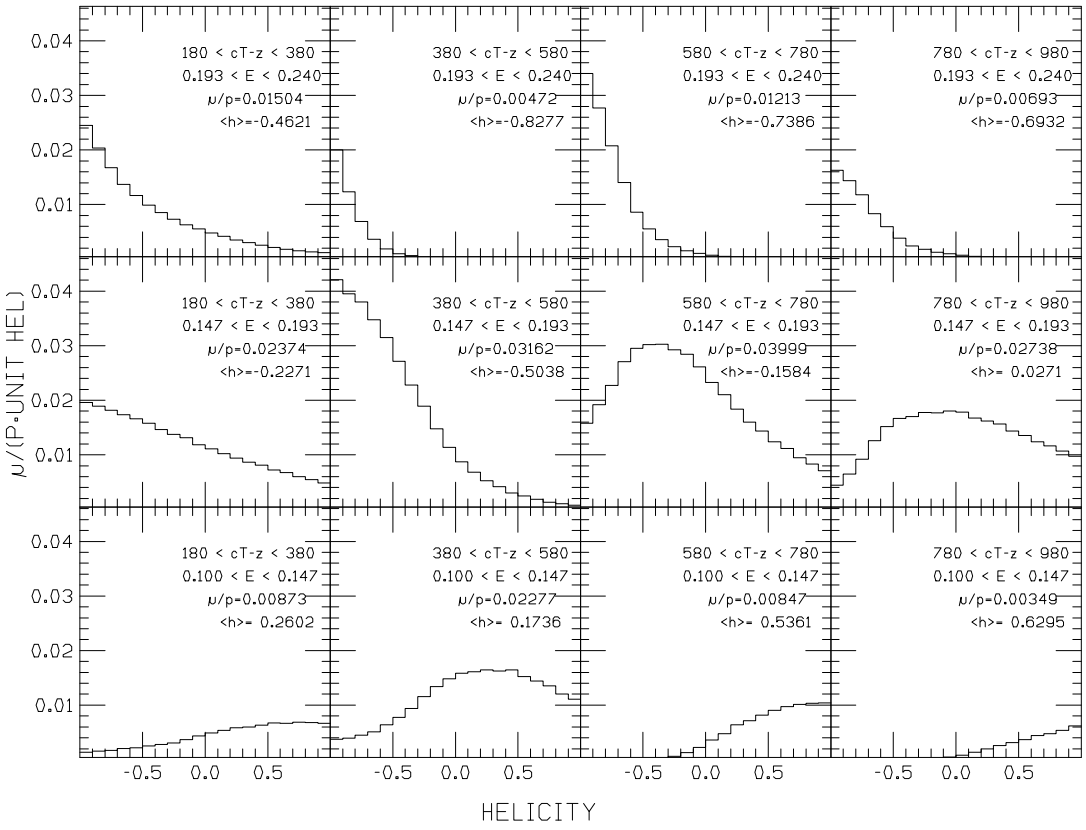

Figure 6: Helicity distribution in subregions of E–t space, delineated by cT-z (in cm) and E (in GeV) indicated in legend, for μ^+ collected in *wide* channel with 1 *nsec* long proton beam incident on tilted target. Total muon yield and average helicity in each region are also shown.

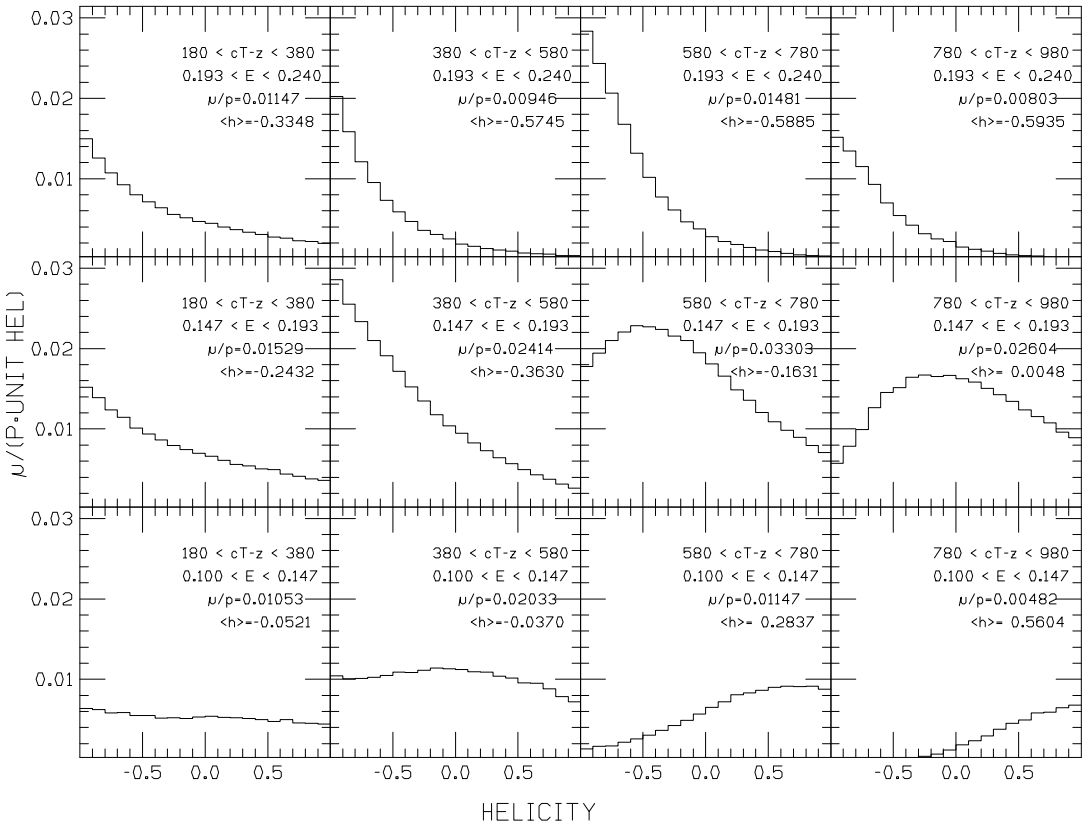

Figure 7: Helicity distribution in subregions of E–t space, delineated by cT-z (in *cm*) and E (in *GeV*) indicated in legend, for μ^+ collected in *wide* channel with 3 *nsec* long proton beam incident on tilted target. Total muon yield and average helicity in each region are also shown.